

Measurement of $^{nat}\text{Pb}(\nu_e, Xn)$ production with a stopped-pion neutrino source

P. An,^{1,2} C. Awe,^{1,2} P.S. Barbeau,^{1,2} B. Becker,³ S.W. Belling,^{2,*} V. Belov,^{4,5} I. Bernardi,³ C. Bock,⁶ A. Bolozdynya,⁴ R. Bouabid,^{1,2} A. Brown,^{7,2} J. Browning,⁸ B. Cabrera-Palmer,⁹ M. Cervantes,¹ E. Conley,¹ J. Daughhetee,¹⁰ J. Detwiler,¹¹ K. Ding,⁶ M.R. Durand,¹¹ Y. Efremenko,^{3,10} S.R. Elliott,¹² L. Fabris,¹⁰ M. Febbraro,¹⁰ A. Gallo Rosso,¹³ A. Galindo-Uribarri,^{10,3} M.P. Green,^{2,10,8} J. Hakenmueller,¹ M.R. Heath,¹⁰ S. Hedges,^{1,2,14,†} M. Hughes,¹⁵ B.A. Johnson,¹⁵ T. Johnson,^{1,2} A. Khromov,⁴ A. Konovalov,⁴ E. Kozlova,^{4,5} A. Kumpan,⁴ O. Kyzylova,¹⁶ L. Li,^{1,2} J.M. Link,¹⁶ J. Liu,⁶ A. Major,¹ K. Mann,⁸ D.M. Markoff,^{7,2} J. Mastrobetti,¹⁵ J. Mattingly,¹⁷ K. Miller,^{1,2,‡} P.E. Mueller,¹⁰ J. Newby,¹⁰ D.S. Parno,¹⁸ S.I. Penttila,¹⁰ D. Pershey,¹ C.G. Prior,^{1,2} R. Rapp,^{18,§} J. Raybern,¹ O. Razuvaeva,^{4,5} D. Reyna,⁹ G.C. Rich,² J. Ross,^{7,2} D. Rudik,⁴ J. Runge,^{1,2} D.J. Salvat,¹⁵ A.M. Salyapongse,¹⁸ J. Sander,⁶ K. Scholberg,¹ A. Shakirov,⁴ G. Simakov,^{4,5} G. Sinev,^{1,¶} W.M. Snow,¹⁵ V. Sosnovtsev,⁴ T. Subedi,¹⁶ B. Suh,¹⁵ R. Tayloe,¹⁵ K. Tellez-Giron-Flores,¹⁶ E. Ujah,^{7,2} J. Vanderwerp,¹⁵ E.E. van Nieuwenhuizen,^{1,2} R.L. Varner,¹⁰ C.J. Virtue,¹³ G. Visser,¹⁵ K. Walkup,¹⁶ E.M. Ward,³ T. Wongjirad,¹⁹ J. Yoo,²⁰ C.-H. Yu,¹⁰ and J. Zettlemoyer^{15,**}

¹Department of Physics, Duke University, Durham, NC, 27708, USA

²Triangle Universities Nuclear Laboratory, Durham, NC, 27708, USA

³Department of Physics and Astronomy, University of Tennessee, Knoxville, TN, 37996, USA

⁴National Research Nuclear University MEPhI (Moscow Engineering Physics Institute), Moscow, 115409, Russian Federation

⁵National Research Center “Kurchatov Institute”, Moscow, 123182, Russian Federation

⁶Department of Physics, University of South Dakota, Vermillion, SD, 57069, USA

⁷Department of Mathematics and Physics, North Carolina Central University, Durham, NC, 27707, USA

⁸Department of Physics, North Carolina State University, Raleigh, NC, 27695, USA

⁹Sandia National Laboratories, Livermore, CA, 94550, USA

¹⁰Oak Ridge National Laboratory, Oak Ridge, TN, 37831, USA

¹¹Center for Experimental Nuclear Physics and Astrophysics & Department of Physics, University of Washington, Seattle, WA, 98195, USA

¹²Los Alamos National Laboratory, Los Alamos, NM, 87545, USA

¹³Department of Physics, Laurentian University, Sudbury, Ontario, P3E 2C6, Canada

¹⁴Lawrence Livermore National Laboratory, Livermore, CA, 94550, USA

¹⁵Department of Physics, Indiana University, Bloomington, IN, 47405, USA

¹⁶Center for Neutrino Physics, Virginia Tech, Blacksburg, VA, 24061, USA

¹⁷Department of Nuclear Engineering, North Carolina State University, Raleigh, NC, 27695, USA

¹⁸Department of Physics, Carnegie Mellon University, Pittsburgh, PA, 15213, USA

¹⁹Department of Physics and Astronomy, Tufts University, Medford, MA, 02155, USA

²⁰Department of Physics and Astronomy, Seoul National University, Seoul, 08826, Korea

(Dated: December 23, 2022)

Using neutrinos produced at the Spallation Neutron Source (SNS) at Oak Ridge National Laboratory (ORNL), the COHERENT collaboration has studied the $\text{Pb}(\nu_e, Xn)$ process with a lead neutrino-induced-neutron (NIN) detector. Data from this detector are fit jointly with previously collected COHERENT data on this process. A combined analysis of the two datasets yields a cross section that is $0.29^{+0.17}_{-0.16}$ times that predicted by the MARLEY event generator, consistent with no NIN events at 1.8σ . This is the first inelastic neutrino-nucleus process COHERENT has studied, among several planned exploiting the high flux of low-energy neutrinos produced at the SNS.

Introduction When a sufficiently energetic neutrino interacts with a nucleus, neutrons can be emitted as part of the nuclear de-excitation process. Neutrino-induced

neutrons (NINs) from low-energy neutrinos ($\lesssim 50$ MeV) were predicted in 1978 [1], but have not yet been observed. There is a limited number of existing experimental measurements of low energy neutrino-nucleus interactions through any channel [2], so cross section predictions for many of these interactions are untested. NINs produced through electron neutrino charged-current (CC) interactions on lead nuclei are of particular interest, owing to the large predicted cross section [3–9] and the prevalence of lead as a common shielding material. These interactions can be used to detect supernovae, can impact the nucleosynthesis that occurs during a supernova, and can form a background for neutrino and dark matter experiments.

* Now at: Department of Electrical and Computer Engineering, University of Wisconsin–Madison, Madison, WI, 53706, USA

† hedges3@llnl.gov

‡ Now at: University of Chicago, Chicago, IL, 60637, USA

§ Now at: Washington & Jefferson College, Washington, PA, 15301, USA

¶ Now at: South Dakota School of Mines and Technology, Rapid City, SD, 57701, USA

** Now at: Fermi National Accelerator Laboratory, Batavia, IL, 60510, USA

The majority of existing supernova neutrino detectors are primarily sensitive to the electron-antineutrino component of the supernova neutrino flux through the detection of inverse beta decay interactions on hydrogen [10]. One of the exceptions is the HALO experiment [11, 12], which will detect electron neutrinos emitted by supernovae through the production of NINs on lead. This provides HALO with a unique capability [13], although the NIN cross section on lead must be measured to determine the detector’s sensitivity.

Neutrino-nucleus reactions have been hypothesized to play a role in supernova nucleosynthesis for some time [1]. This can occur either through direct interactions (the ν -process) or through the production and subsequent rapid capture of neutrons (the r -process) [1, 14–17]. A measurement of the NIN cross section for neutrinos of similar energy to those emitted by a supernova would help determine the impact of NINs on the isotopic abundances generated by supernovae.

NIN interactions in shielding material can potentially impact a variety of neutrino and dark matter experiments. In oscillation experiments such as LSND [18], NINs produced by charged-current interactions in shielding may create a background [3]. NINs from solar neutrinos have been proposed to explain the DAMA/LIBRA excess [19], although this claim has been refuted [20, 21]. In searches for coherent elastic neutrino-nucleus scattering (CEvNS), NINs originating from shielding material can produce low energy nuclear recoils in detectors, mimicking the CEvNS signal [22]. In particular, for CEvNS searches at pion decay-at-rest neutrino sources [22, 23], NINs follow the timing distribution of the neutrinos, which can make them problematic.

The COHERENT collaboration has studied the charged-current NIN process on lead using neutrinos produced [24] at the Spallation Neutron Source (SNS) at Oak Ridge National Laboratory (ORNL). As an initial test, the collaboration deployed two 1.5-L liquid scintillator cells inside the shielding used for the COHERENT CsI[Na] detector [22] – this NIN detector is referred to as the Eljen cell detector. The initial measurement from the Eljen cell detector reported a cross section a factor of ~ 1.7 times lower than predicted in reference [6], although there were large uncertainties on the measurement. As a follow-up, two detectors – referred to as the neutrino cubes – were developed and deployed to the SNS in 2015 to measure NIN production on lead and iron. This paper discusses the design of the lead neutrino cube, along with the analysis of a ~ 5 -year exposure, and a combined result with an updated analysis of the Eljen cell detector.

Experimental description: The lead neutrino cube consists of a ~ 900 -kg cast lead target with four cylindrical cavities for liquid scintillator detectors. Two types of liquid scintillator detectors were used throughout this deployment: cylindrical 2.4-liter detectors and hexagonal 1.25-liter detectors. Both types of detectors held EJ-301 scintillator with Electron Tubes 9821-KEB 3” photo multiplier tubes (PMTs). Plastic scintillator-based muon

veto panels were placed against the four sides and top of the lead target to reject muon-induced neutron backgrounds. Near-hermetic modular water shielding surrounded the muon veto panels to reduce environmental and beam-related neutron (BRN) backgrounds. A rendering of the detector is shown in Fig. 1.

The detector was located 18.9 m from the SNS target in “Neutrino Alley”, where it was exposed to an intense flux of low energy (< 52.8 MeV) neutrinos. At the SNS, prompt muon neutrinos are produced from the decay of pions (lifetime of 26 ns), while delayed muon-antineutrinos and electron neutrinos are produced from the decay of stopped positive muons (lifetime of $2.2 \mu\text{s}$). As the FWHM width of the beam timing profile is ≈ 350 ns, the prompt and delayed neutrino fluxes are separated in time, allowing the isolation of ν_e CC NIN events from beam-related backgrounds. More details on Neutrino Alley and the neutrinos produced at the SNS can be found in reference [22].

The data used for the analysis were collected between January 2016 and January 2021. The detector operated in three different configurations, i.) with four cylindrical detectors present, ii.) with two cylindrical detectors present, and iii.) with two cylindrical and two hexagonal detectors present. The detector was monitored for stable running conditions and periods with detector electronics issues or atypical beam operations were removed from the analysis. Combining data from all configurations, the lead neutrino cube collected NINs produced in the surrounding lead over an exposure of 127 GWhr-liters.

The lead neutrino cube triggers on the coincidence of a signal from any of the liquid scintillator cells above a level-threshold and a timing signal generated by the SNS. The timing signal is synchronized to the proton pulse timing at the SNS and can be reliably used to determine the neutrino generation time. When a coincidence is detected within a $\sim 20 \mu\text{s}$ window, $80 \mu\text{s}$ waveforms are recorded from all channels (liquid scintillators, vetoes, and SNS timing signals) with the trigger occurring 35% of the way through the waveform.

A conditional moving average filter [25] is used to remove long-timescale oscillations in the baseline of waveforms. To determine the start-time of the pulse, a smoothing interpolation algorithm [26] is applied to achieve an onset (t_0) for each pulse with sub-sample precision, where the onset is defined as 20% of the maximum pulse amplitude. A 400 ns window is integrated around the pulse onset (10 ns prior to onset, 390 ns after) to determine the energy of the pulse. A pulse-shape discrimination (PSD) parameter is calculated as the ratio of the tail integral to the full integral of the pulse, where the tail integral length was optimized for each channel and varied from the last 355 to 360 ns of the integral window.

Cosmic events passing through the muon veto are identified by requiring a coincident signal in two or more PMTs from the muon veto panels within a 200 ns window. Events in a liquid scintillator cell preceding the muon veto signal by up to 200 ns or following within a $25 \mu\text{s}$

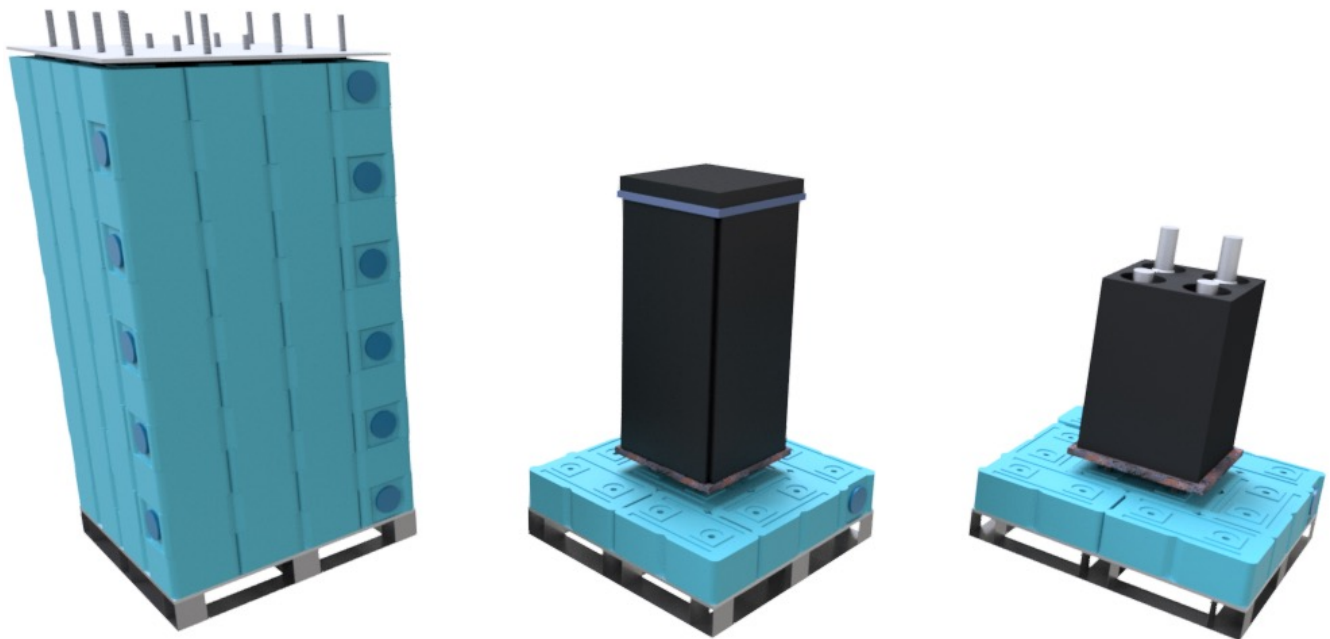


FIG. 1. Left: exterior view of the neutrino cube showing water bricks used to reduce neutron backgrounds. Center: Cut-away view showing the muon veto panels inside the water shielding. Right: Cut-away view showing the lead target and liquid scintillator detectors. The bottom of the liquid scintillator detectors is located approximately at the midpoint of the lead target.

window are identified as muon-correlated events and are removed.

Events preceding the SNS timing signal by up to $2\ \mu\text{s}$ or following the timing signal by up to $12\ \mu\text{s}$ were blinded during the analysis to avoid developing cuts that bias the results.

Calibrations were performed with dedicated gamma source runs to set the energy scale of each detector. These sources were simulated in MCNPX-PoliMI [27] and fit to the data, allowing the conversion from ADC-to-keV and energy resolution parameters to float. Relative changes in the gain of each detector were tracked between gamma calibrations by fitting the background spectrum above the Compton endpoint of environmental 511-keV γ -rays. PSD parameters and trigger efficiencies were studied with neutrons from a dedicated *in-situ* run using a time-tagged ^{252}Cf source. More detailed discussion of the calibrations of the neutrino cube detector may be found in the supplemental material.

The energy threshold of the pulse identification algorithm was determined by plotting pulse height versus integral and fitting the relationship as a function of energy. This was done separately for gamma and neutron events using the time-tagged ^{252}Cf calibration source data. By incorporating individual detector gain changes and exposures, a weighted efficiency curve for the detector was produced as a function of recoil energy, shown in Fig. 2.

The pulse-shape distributions of events in the liquid scintillator cells were observed to vary with time – this can be the result of PMT aging, oxygen leaking into the

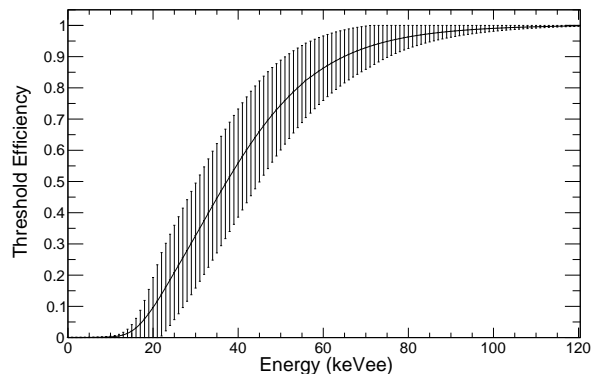


FIG. 2. Neutron pulse identification threshold function from all liquid scintillators weighted by each cell's exposure. Errors are derived from the uncertainties on parameters in the fits of pulse height versus integral.

liquid scintillator, or helium leaking into the PMTs [28]. The variation in the pulse-shape distributions was corrected by fitting the mean of the gamma PSD distribution and scaling PSD parameters so that the gamma mean always occurred at the same PSD value. The corrected pulse-shape distributions from the production data were fit using energy-dependence functions from the ^{252}Cf calibrations with floating parameters. An energy-dependent cut on the PSD parameter was imposed to maximize the sensitivity of the detector. The lowest energy for which

Channel	Cross section ($\times 10^{-40} \text{ cm}^2$)
$^{208}\text{Pb}(\nu_e, X)$	42.1
$^{208}\text{Pb}(\nu_e, e^- + n)^{207}\text{Bi}$	31.6
$^{208}\text{Pb}(\nu_e, e^- + 2n)^{206}\text{Bi}$	7.7
$^{208}\text{Pb}(\nu_e, e^- + 3n)^{205}\text{Bi}$	0.4

TABLE I. Predictions of charged-current cross sections for ^{208}Pb using decay-at-rest electron neutrinos with MARLEY configured with $B(\text{GT}^-)$ data from reference [32]. Interaction channels which do not produce a final-state neutron are included in the $^{208}\text{Pb}(\nu_e, X)$ value. For lead of naturally-occurring isotopic abundances, imposing $N - Z$ scaling produces an inclusive flux-averaged cross section of $41.4 \times 10^{-40} \text{ cm}^2$.

good separation between gammas and neutrons could be determined varied for each detector, from 90 to 170 keV. A typical PSD distribution, along with a weighted PSD cut efficiency curve, is depicted in Fig. 3. The discontinuities in the weighted efficiency curve arise from variations in the lower PSD threshold achieved for each of the detectors.

Signal prediction: Predictions for the charged-current signal were obtained using MARLEY [29, 30]. While MARLEY was developed for generating charged-current signals on argon [31], it can be utilized for other nuclei by supplying distributions of the Gamow-Teller (GT^-) and Fermi (F) strength. For lead, GT^- strengths were obtained from the data in reference [32] provided for use by the authors. The GT^- strengths were scaled by $g_A^2 = (1.26)^2$ to account for the different definition of matrix elements in charge-exchange and weak interactions, and the energy scale was adjusted to account for the difference in the ground state energy of ^{208}Pb and ^{208}Bi . MARLEY does not include contributions from forbidden transitions, which will increase the predicted cross section and change the distribution of generated particles produced in charged-current events. The Fermi strength was obtained using the Fermi sum rule, $B(F) = N - Z$, with an energy centered on the isobaric analog state of ^{208}Pb in ^{208}Bi [33]. The predicted inclusive MARLEY flux-averaged cross section for decay-at-rest electron neutrino charged-current interactions with ^{208}Pb is $42.1 \times 10^{-40} \text{ cm}^2$, in good agreement with existing predictions [3–9, 34].

As in reference [3], a $N - Z$ scaling was assumed for the naturally occurring isotopes of lead in the signal calculation. The inclusive cross section from MARLEY for ^{208}Pb , along with the partial cross sections leading to neutron emission, are shown in Tab. I.

Neutral-current predictions were also calculated with MARLEY, using $B(M1)$ strength distributions from [35, 36] and an assumed conversion from $B(M1)$ to $B(\text{GT}_0)$ from reference [37]. However, the predicted neutral-current neutron emission cross section was only $\approx 1.6\%$ of the predicted charged-current cross section, so these events were not included as a component in the fit. As a

comparison, the neutral-current component expected in HALO is larger as all six flavors of neutrino contribute to the rate while only three contribute at the SNS.

The charged-current events generated by MARLEY were simulated originating from the lead target using GEANT4 [38] to determine an average efficiency of reaching the liquid scintillator cells of 18.8%. The simulation output was processed matching analysis choices and cuts, employing measured energy resolution functions and EJ-301 quenching factors from references [39, 40]. Applying these reduces the average efficiency to 3.3%. While MARLEY does not interface directly with MCNP, as a cross-check neutrons were simulated in 500-keV bins in MCNPX-PoliMi. Despite the coarse energy binning, the MCNP neutron detection efficiency agrees with that from GEANT4 to within 4.3%.

Calculations in reference [24] were used to determine the expected number of neutrinos generated as a function of proton energy and beam power at the SNS. Using the nominal MARLEY cross section and simulated efficiencies, 346 charged-current NIN events were expected in the analyzed data set.

Results and discussion: The primary challenge in identifying NIN events above threshold is discriminating between neutrino-induced neutrons and prompt beam-related neutron (BRN) backgrounds. Both produce proton recoils and thus have similar PSD distributions. The recoil energy distributions of the two populations are also similar. However, NINs and BRNs occur at different times. Thus, a 1D fit in recoil time was performed to determine the NIN signal and prompt background counts. All counts with a reconstructed energy less than 425-825 keV $_{ee}$ that pass the PSD selection cut were included in the fit. The upper energy limit of the fit was determined for each detector to optimize the separation of NIN signal and steady-state alpha backgrounds, which can have a neutron-like PSD.

A number of sources of systematic uncertainty were evaluated. Eight sources were identified that affect our determination of the NIN cross section which are included in the result and listed in Tab. II. The dominant normalization uncertainty originates in the uncertainty in the neutrino flux at the SNS which will be improved with future COHERENT data [41]. Quenching and calibration uncertainties are the next largest sources, each affecting the cross section by 2 – 3%. The timing of the NIN pulse was determined from measurements of the beam current at the SNS with an uncertainty of ~ 38 ns.

The normalization of the prompt beam-related neutron background was allowed to float freely. However, since the timing distribution of these events is critical for determining the NIN rate, the mean and width of the neutron timing pulse were included as unconstrained parameters in the fit. Measured neutron time-of-flight depends on detector location within Neutrino Alley and threshold, which governs the neutron energy range that produced the background, so past neutron data from COHERENT may not accurately constrain these uncertain-

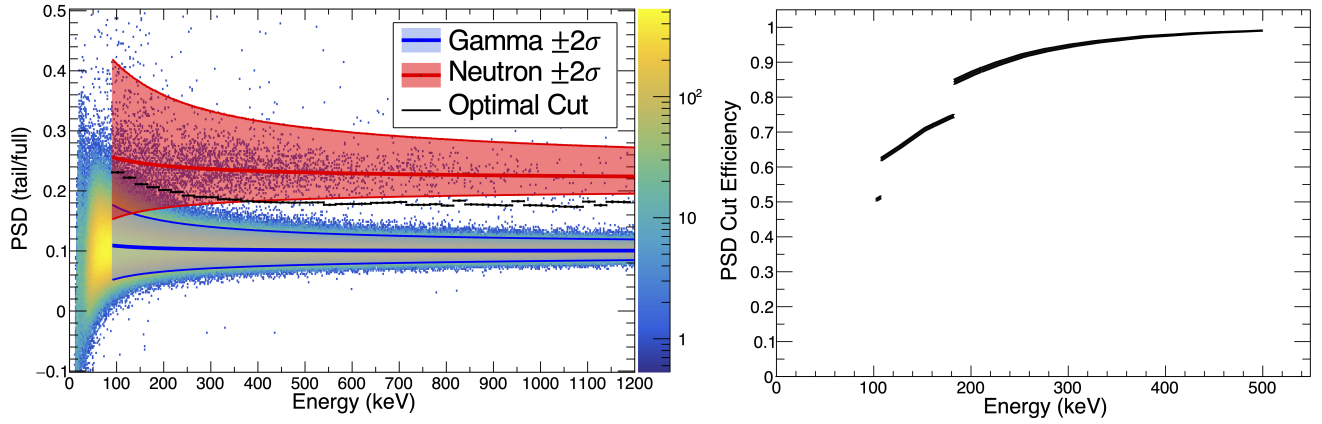


FIG. 3. Left: PSD distribution for ^{252}Cf events tagged in a single liquid scintillator detector, with the 2σ neutron acceptance region shown in red, and that for gammas in blue. The black line shows the optimal PSD cut used in the analysis for this channel. Right: The optimized PSD cut for each channel is weighed by that channel's exposure to produce a PSD efficiency curve for the lead neutrino cube. The discontinuities arise from the variation in lower energy of the PSD threshold achieved for each detector.

Source	NIN uncertainty (%)
Neutrino flux	± 10
Quenching factor	± 2.7
Software threshold	$+0.2 / -0.4$
PSD selection	± 1.0
Calibration	$+2.1 / -2.2$
Energy resolution	$+1.7 / -0.5$
Muon veto	$+0.4 / -0.3$
Lead target mass	± 0.6
MARLEY NC prediction	$+0 / -1.6$
Total:	$+10.8 / -10.8$

TABLE II. Summary of sources of systematic uncertainty which affect the NIN normalization.

ties. The width of the prompt pulse may be wider than the protons-on-target (POT) trace (full-width half maximum (FWHM) nominally $\sim 350\text{ns}$) due to variations in neutron time-of-flight. This broadening is incorporated into the fit by convolving the POT trace with a Gaussian smearing of prompt neutron arrival times. The standard deviation of the Gaussian is treated as a free parameter.

After determining reconstruction, selection, and analysis methods, the data were unblinded, resulting in the spectrum shown in Fig. 4. The data selected by the cuts were fit to determine the NIN normalization. Two independently developed fitting codes evaluated the data to confirm consistency of the analysis procedure. An unbinned likelihood fit revealed 36^{+72}_{-36} NIN events in the sample, while a binned likelihood fit of the same data found 37^{+69}_{-37} NIN events allowed at 1σ , with both fits showing consistent results. The fit estimated $1,295^{+44}_{-48}$ prompt neutron events with an additional 79^{+11}_{-11} ns of smearing in arrival time. The inferred NIN rate is $> 4\sigma$ lower than expectations from the MARLEY prediction.

As this result is discrepant with expectations, several

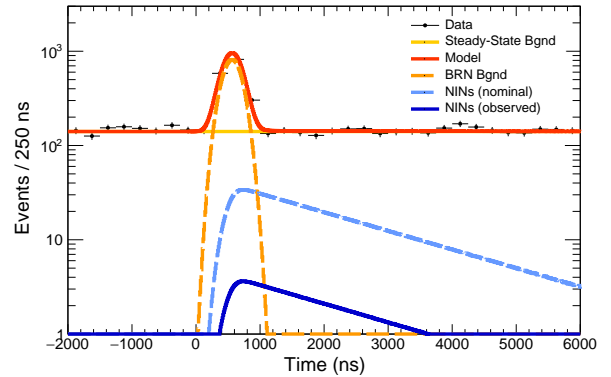


FIG. 4. Timing distribution of observed data within the SNS beam window along with detector background and the predicted and best-fit NIN contributions. The data are consistent with the no-NIN scenario with a 1σ range of 37^{+72}_{-37} NIN counts.

checks were subsequently performed. First, to verify the transparency to neutrons of the lead, the lead used for the target was checked for impurities. The presence of lighter atoms in the surrounding lead may increase the neutron scattering cross section and would also decrease the density of the neutrino target. The lead is stamped as 99.99% natural lead. The density of lead used to cast the targets was measured and determined to be $11.48 \pm 0.21 \text{ g/cm}^3$, within uncertainty of the nominal value of 11.29 g/cm^3 . Second, the prompt neutron event rate was compared to the delivered proton beam power as a function of time. This was done to check the stability of the neutron selection efficiency during detector operations. The excess of neutron events in the prompt window was observed to follow the delivered POT exposure. Third, the PSD cut was extended to include lower

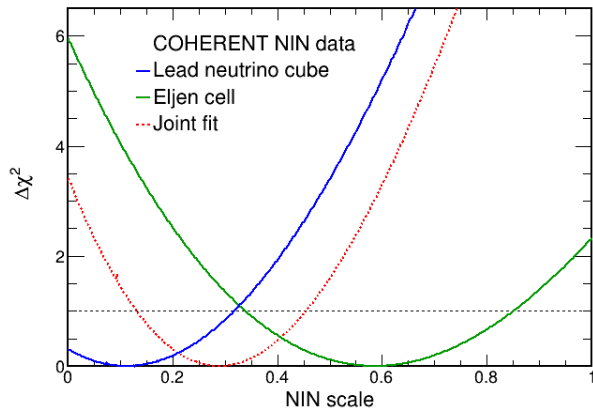


FIG. 5. Likelihood profiles from the lead neutrino cube and Eljen cell detector updated analysis. A value of 1 corresponds to the predicted signal from the MARLEY event generator.

energy recoils. This increases both the expected number of detected neutrons and the sensitivity to lower energy neutrons. Extending the PSD cut down to 50 keV increased the number of expected NINs by a factor of 1.43. However, these lower energy recoil events were not included in the original fit as the uncertainty on their selection efficiency is large. Fitting this low recoil energy sideband gave a NIN rate consistent with that observed in the analysis sample.

The analysis of the Eljen cell data in reference [22] has been updated in three ways. The previous analysis assumed that the emitted NINs followed an evaporative neutron spectrum, and assumed the spectra of neutron emission events of all multiplicities were identical. The updated analysis has used MARLEY to generate a neutron energy distribution that depends on the multiplicity of the event along with new calculations of the number of neutrinos produced per incident POT from reference [24]. Finally, time broadening of the beam-related neutron population was incorporated into the fit and allowed to float, as was done in the analysis of the lead neutrino cube, to incorporate dispersion effects due to time-of-flight varying with incident neutron energy. The influence of this additional uncertainty is detailed in supplementary materials [42].

Combining the results yields a cross section scaling factor of $0.29^{+0.17}_{-0.16}$ relative to predictions from MARLEY (see Tab. I) from a joint fit. For the neutrino cube sample, this corresponds to 100^{+57}_{-54} events, consistent with the NIN fit using only data from this detector.

The lead neutrino cube was designed to measure the $^{nat}\text{Pb}(\nu_e, e^- + Xn)$ cross section using electron neutrinos produced at the SNS. The origin of the observed reduction in the signal expectations is unknown. It should be noted that while the suppression is observed in the measured results compared to the MARLEY model, the current result cannot provide meaningful data on charged-current events on lead without neutron emission, as the

detector is not designed to measure the emitted electron.

One possible explanation could be that the inclusive charged-current cross section is lower than expected for lead, affecting both neutron emitting and non-neutron emitting interactions. This could be tested by a dedicated detector measuring the electromagnetic energy deposited in charged-current events on lead. This can be done within COHERENT, and there are also external plans (see reference [43]). Additionally, a detector measuring the electromagnetic component of charged-current neutrino interactions on ^{127}I has collected data for several years at the SNS, and may help to test theoretical predictions.

Another possibility is that the neutrons emitted by the charged-current interaction have energies lower than theoretically predicted in MARLEY. If this is the case, the sensitivity of the HALO experiment would be unaffected by the observed reduction in the charged-current cross section. However, there are no models predicting the emission of low energy neutrons from charged-current events on lead. A measurement of the NIN cross section with a capture-gated detector would test this possibility.

Measuring the NIN cross section on a lighter target may also provide understanding for the current result. In 2017, a similar detector to the lead neutrino cube was deployed to the SNS, seeking to measure the NIN cross section on iron with a ~ 700 -kg target. The results described herein reduce the likelihood that the iron neutrino cube will successfully measure the NIN cross section, but analysis is still under way on the data it has collected.

There are several implications of a reduced lead NIN cross section for existing experiments. For CEvNS detectors at the SNS and ESS, this measurement impacts the expected backgrounds and design of detector shielding. This result has negative implications for HALO's potential to study supernova neutrinos. However, the HALO data continues to be vital for understanding the next galactic core-collapse supernova as HALO is sensitive to the ν_e component of the supernova flux, while most large detectors are primarily sensitive to the $\bar{\nu}_e$ component through inverse beta decay.

A separate analysis of the $2n$ NIN emission cross section on lead is planned using the data collected by the lead neutrino cube. While the rate of observed events is expected to be lower, steady-state backgrounds are also significantly reduced.

Conclusion: Five years of data have been recorded and analyzed to study NINs produced from electron neutrino charged-current interactions on lead at the SNS. Combining the results of this analysis with an updated analysis of the Eljen cell detector yields a cross section suppressed by a factor of $0.29^{+0.17}_{-0.16}$ compared to the MARLEY prediction. The cause of the apparent reduction in the NIN cross section is unknown, but future experiments will help to determine its origin. Within COHERENT, updated measurements of the neutrino flux with a heavy-water detector will improve systematic uncer-

tainties on the existing measurements [41], and measurements of charged-current cross sections on other targets may help to determine whether a similar suppression is seen for other nuclei.

Acknowledgements: The COHERENT collaboration would like to thank the Duke Machine Shop for its help casting the lead targets used for this detector, Steven Gardiner for his assistance in adapting MARLEY for use with iron and lead, and the authors of reference [32] for providing the $^{208}\text{Pb}(p, n)$ data used for generating predictions with MARLEY.

The COHERENT collaboration acknowledges the Kavli Institute at the University of Chicago for Eljen cell detector contributions. The COHERENT collaboration acknowledges the generous resources provided by the ORNL Spallation Neutron Source, a DOE Office of Science User Facility, and thanks Fermilab for the con-

tinuing loan of the CENNS-10 detector. We also acknowledge support from the Alfred P. Sloan Foundation, the Consortium for Nonproliferation Enabling Capabilities, the National Science Foundation, the Korea National Research Foundation (NRF 2022R1A3B1078756), and the U.S. Department of Energy, Office of Science. Laboratory Directed Research and Development funds from ORNL also supported this project. This work was performed under the auspices of the U.S. Department of Energy by Lawrence Livermore National Laboratory under Contract DE-AC52-07NA27344. This research used the Oak Ridge Leadership Computing Facility, which is a DOE Office of Science User Facility. The work was supported by the Ministry of Science and Higher Education of the Russian Federation, Project Fundamental properties of elementary particles and cosmology No. 0723-2020-0041.

-
- [1] G. V. Domogatskii and D. K. Nadëzhin, *Sov. Astron.* **22**, 297 (1978).
 - [2] J. A. Formaggio and G. P. Zeller, *Rev. Mod. Phys.* **84**, 1307 (2012), URL <https://link.aps.org/doi/10.1103/RevModPhys.84.1307>.
 - [3] E. Kolbe and K. Langanke, *Phys. Rev. C* **63**, 025802 (2001), URL <https://link.aps.org/doi/10.1103/PhysRevC.63.025802>.
 - [4] C. Volpe et al., *Phys. Rev. C* **65**, 044603 (2002), URL <https://link.aps.org/doi/10.1103/PhysRevC.65.044603>.
 - [5] T. Suzuki and H. Sagawa, *Nucl. Phys. A* **718**, 446 (2003).
 - [6] G. C. McLaughlin, *Phys. Rev. C* **70**, 045804 (2004), ISSN 05562813.
 - [7] M. S. Athar, S. Ahmad, and S. Singh, *Nuc. Phys. A* **764**, 551 (2006), ISSN 0375-9474, URL <https://www.sciencedirect.com/science/article/pii/S0375947405011334>.
 - [8] R. Lazauskas and C. Volpe, *Nucl. Phys. A* **792**, 219 (2007), ISSN 0375-9474, URL <https://www.sciencedirect.com/science/article/pii/S0375947407005775>.
 - [9] N. Paar et al., *Phys. Rev. C* **77**, 024608 (2008), URL <https://link.aps.org/doi/10.1103/PhysRevC.77.024608>.
 - [10] A. G. Rosso et al., *New J. Phys.* **23**, 031201 (2021).
 - [11] K. Zuber, *Nuclear and Particle Physics Proceedings* **265-266**, 233 (2015), ISSN 2405-6014, proceedings of the Neutrino Oscillation Workshop, URL <https://www.sciencedirect.com/science/article/pii/S2405601415004010>.
 - [12] C. A. Duba et al., *Journal of Physics: Conference Series* **136**, 042077 (2008), URL <https://doi.org/10.1088/1742-6596/136/4/042077>.
 - [13] A. G. Rosso, *Journal of Cosmology and Astroparticle Physics* **06**, 046 (2021), URL <https://dx.doi.org/10.1088/1475-7516/2021/06/046>.
 - [14] S. Woosley et al., *The Astrophysical Journal* **356**, 272 (1990).
 - [15] A. Sieverding et al., *The Astrophysical Journal* **865**, 143 (2018), URL <https://doi.org/10.3847/1538-4357/aadd48>.
 - [16] G. C. McLaughlin and G. M. Fuller, *The Astrophysical Journal* **464**, L143 (1996), astro-ph/9603082.
 - [17] Y. Qian et al., *Phys. Rev. C* **55** (1997), URL <https://www.osti.gov/biblio/524960>.
 - [18] G. B. Mills, *Nuc. Phys. B - Proceedings Supplements* **66**, 382 (1998), ISSN 0920-5632, proceedings of the XVI Workshop on Weak Interactions and Neutrinos, URL <https://www.sciencedirect.com/science/article/pii/S0920563298000693>.
 - [19] J. H. Davis, *Phys. Rev. Lett.* **113**, 081302 (2014), URL <https://link.aps.org/doi/10.1103/PhysRevLett.113.081302>.
 - [20] P. S. Barbeau et al., *Phys. Rev. Lett.* **113**, 229001 (2014), URL <https://link.aps.org/doi/10.1103/PhysRevLett.113.229001>.
 - [21] R. Bernabei et al., *The European Physical Journal C* **74**, 3196 (2014), ISSN 1434-6052, URL <https://doi.org/10.1140/epjc/s10052-014-3196-5>.
 - [22] D. Akimov et al., *Science* **357**, 1123 (2017).
 - [23] D. Baxter et al., *J. High Energ. Phys.* **2020**, 123 (2020), URL [https://doi.org/10.1007/JHEP02\(2020\)123](https://doi.org/10.1007/JHEP02(2020)123).
 - [24] D. Akimov et al. (COHERENT Collaboration), *Phys. Rev. D* **106**, 032003 (2022), URL <https://link.aps.org/doi/10.1103/PhysRevD.106.032003>.
 - [25] G. C. Rich, Ph.D. thesis, University of North Carolina, Chapel Hill (2017).
 - [26] W. K. Warburton and W. Hennig, *IEEE Transactions on Nuclear Science* **64**, 2938 (2017).
 - [27] S. A. Pozzi, E. Padovani, and M. Marseguerra, *Nuclear Instruments and Methods in Physics Research Section A: Accelerators, Spectrometers, Detectors and Associated Equipment* **513**, 550 (2003), ISSN 0168-9002, URL <http://www.sciencedirect.com/science/article/pii/S0168900203023027>.
 - [28] Hamamatsu Photonics, *Photomultiplier tubes, 4th Edition* (Hamamatsu Photonics, 2017), URL https://www.hamamatsu.com/content/dam/hamamatsu-photonics/sites/documents/99_SALES_LIBRARY/etd/PMT_handbook_v4E.pdf.
 - [29] S. Gardiner, *MARLEY (Model of Argon Reaction Low*

- Energy Yields*) (2021), URL <https://doi.org/10.5281/zenodo.3905443>.
- [30] S. Gardiner, Computer Physics Communications **269**, 108123 (2021), ISSN 0010-4655, URL <https://www.sciencedirect.com/science/article/pii/S0010465521002356>.
 - [31] S. Gardiner, Phys. Rev. C **103**, 044604 (2021), URL <https://link.aps.org/doi/10.1103/PhysRevC.103.044604>.
 - [32] T. Wakasa et al., Phys. Rev. C **85**, 064606 (2012), URL <https://link.aps.org/doi/10.1103/PhysRevC.85.064606>.
 - [33] F. Osterfeld, Rev. Mod. Phys. **64**, 491 (1992), URL <https://link.aps.org/doi/10.1103/RevModPhys.64.491>.
 - [34] J. Engel, G. C. McLaughlin, and C. Volpe, Phys. Rev. D **67**, 013005 (2003), URL <https://link.aps.org/doi/10.1103/PhysRevD.67.013005>.
 - [35] I. Poltoratska et al., Phys. Rev. C **85**, 041304 (2012), URL <https://link.aps.org/doi/10.1103/PhysRevC.85.041304>.
 - [36] J. Birkhan et al., Phys. Rev. C **93**, 041302 (2016), URL <https://link.aps.org/doi/10.1103/PhysRevC.93.041302>.
 - [37] S. V. Semenov, Bulletin of the Russian Academy of Sciences: Physics **81**, 735 (2017).
 - [38] S. Agostinelli et al., Nuclear Instruments and Methods in Physics Research Section A: Accelerators, Spectrometers, Detectors and Associated Equipment **506**, 250 (2003), ISSN 0168-9002, URL <https://www.sciencedirect.com/science/article/pii/S0168900203013688>.
 - [39] C. Awe et al., Phys. Rev. C **98**, 045802 (2018), URL <https://link.aps.org/doi/10.1103/PhysRevC.98.045802>.
 - [40] V. Verbinski et al., Nuclear Instruments and Methods **65**, 8 (1968), ISSN 0029-554X, URL <https://www.sciencedirect.com/science/article/pii/0029554X68900037>.
 - [41] D. Akimov et al. (COHERENT), JINST **16**, P08048 (2021), 2104.09605.
 - [42] See Supplemental Material at URL [will_be_inserted_by_publisher](#) for a detailed explanation of Neutrino cube calibrations.
 - [43] F. Suekane et al., *Conceptual Design Report of DaRveX: Decay at Rest ν_e + Lead Cross Section Measurement at J-PARC MLF* (2022), URL <https://arxiv.org/abs/2205.11769>.
 - [44] G. Dietze and H. Klein, Nuclear Instruments and Methods in Physics Research **193**, 549 (1982), ISSN 0167-5087, URL <https://www.sciencedirect.com/science/article/pii/0029554X8290249X>.
 - [45] D. Foreman-Mackey et al., Publ. of the Astro. Society of the Pacific **125**, 306 (2013).
 - [46] F. Arneodo et al., Nuclear Instruments and Methods in Physics Research Section A: Accelerators, Spectrometers, Detectors and Associated Equipment **418**, 285 (1998), ISSN 0168-9002, URL <https://www.sciencedirect.com/science/article/pii/S0168900298006792>.
 - [47] D. Schmidt et al., Nuclear Instruments and Methods in Physics Research Section A: Accelerators, Spectrometers, Detectors and Associated Equipment **476**, 186 (2002), ISSN 0168-9002, int. Workshop on Neutron Field Spectrometry in Science, Technology and Radiation Protection, URL <https://www.sciencedirect.com/science/article/pii/S0168900201014280>.
 - [48] R. Byrd et al., Nuclear Instruments and Methods in Physics Research Section A: Accelerators, Spectrometers, Detectors and Associated Equipment **313**, 457 (1992), ISSN 0168-9002, URL <https://www.sciencedirect.com/science/article/pii/016890029290824N>.
 - [49] H. Klein and S. Neumann, Nuclear Instruments and Methods in Physics Research Section A: Accelerators, Spectrometers, Detectors and Associated Equipment **476**, 132 (2002), ISSN 0168-9002, int. Workshop on Neutron Field Spectrometry in Science, Technology and Radiation Protection, URL <https://www.sciencedirect.com/science/article/pii/S0168900201014103>.
 - [50] W. Verkerke and D. P. Kirkby, eConf **C0303241**, MOLT007 (2003), physics/0306116.

I. APPENDIX: CALIBRATIONS

A. Dedicated gamma source calibrations

Several times throughout the detector's operational period, energy calibrations were performed using dedicated runs with a radioactive source present including running with ^{22}Na , ^{137}Cs , ^{60}Co , and ^{133}Ba sources. These calibrations occurred irregularly throughout operation, as they require partial disassembly of the detector.

The light output in liquid scintillators for electronic interactions is linear above ~ 40 keV [44]. The relationship between light output and true energy is described in Eq. A1.

$$L = c(E_e - E_0) \quad (\text{A1})$$

Here, L is the light output, c is a proportionality constant, E_e is the true energy in keV, and E_0 is a small offset accounting for non-linearity of the light output at low energies [44]. E_0 was fixed to a value of 5 keV [46–49]. Energy resolution impacts the linear calibration parameter, and must be included in a fit to accurately calibrate the detectors.

The energy resolution of a detector at an energy E can be parameterized as

$$\frac{\Delta E}{E} = \sqrt{\alpha_0^2 + \frac{\beta_0^2}{E} + \frac{\gamma_0^2}{E^2}} \quad (\text{A2})$$

where ΔE is the FWHM of a Gaussian centered at E . The parameters $(\alpha_0, \beta_0, \gamma_0)$ originate from different aspects of the light production [44]:

- α_0 is related to location of scintillation light production and transport of light to the photocathode.
- β_0 is related to the statistical behavior of light production.
- γ_0 is a noise term originating in dark counts from the photomultiplier tube and noise introduced in the amplification process.

Gaussian smearing was applied to simulated events, where sigma was solved for in Eq. A2 using the assumption that $\Delta E = 2.355\sigma$.

$$\sigma = \sqrt{\frac{\alpha_0^2 E^2}{2.355^2} + \frac{\beta_0^2 E}{2.355^2} + \frac{\gamma_0^2}{2.355^2}} \quad (\text{A3})$$

The factor of 2.355 was included in the definition of the constants, allowing Eq. A3 to take the form of Eq. .

$$\sigma = \sqrt{\alpha^2 E^2 + \beta^2 E + \gamma^2} \quad (\text{A4})$$

To calibrate detectors, simulations were performed using MCNPX-PoliMi [27] using the full detector geometry and location of the radioactive sources, and the ENSDF source simulation option within MCNPX-PoliMi. The

simulated data were combined with a background spectrum obtained during the calibration run and fit to the radioactive source data. The MCMC software emcee [45] was used to sample three energy resolution parameters, an ADC-to-keV conversion factor, and amplitudes of background and simulated source components. When data were collected with multiple gamma sources during a calibration, separate negative log-likelihoods were generated for each source using the sampled parameters, and these values were combined. The fitting region was chosen where the trigger efficiency was $\sim 100\%$ to avoid incorporating trigger efficiency into the fit. The energy resolution parameters from individual calibrations were combined to yield the parameters used in this analysis, summarized in Tab. III. An example fit of smeared and calibrated simulations along with source data can be found in Fig. 6.

TABLE III. Energy resolution parameters. Channels 0-3 are cylindrical cells, and channels 12 and 13 are hex cells.

Channel	Alpha (unit-less)	Beta ($\sqrt{\text{keV}}$)	Gamma (keV)
0	$0.101^{+0.004}_{-0.004}$	$0.356^{+0.213}_{-0.210}$	$4.543^{+2.451}_{-2.464}$
1	$0.102^{+0.004}_{-0.004}$	$0.794^{+0.473}_{-0.398}$	$12.565^{+4.587}_{-4.998}$
2	$0.093^{+0.021}_{-0.006}$	$0.668^{+0.404}_{-0.328}$	$11.890^{+12.993}_{-4.464}$
3	$0.093^{+0.008}_{-0.008}$	$1.584^{+0.238}_{-0.316}$	$13.222^{+4.093}_{-4.791}$
12	$0.071^{+0.013}_{-0.011}$	$0.793^{+0.147}_{-0.243}$	$11.810^{+2.382}_{-3.041}$
13	$0.069^{+0.005}_{-0.005}$	$0.519^{+0.205}_{-0.255}$	$6.910^{+2.929}_{-3.297}$

B. Relative gain changes

The dedicated gamma source calibrations allow a conversion from ADC-to-keV to be known at the time of the calibration. However, this conversion factor was observed to change over time. Potential sources of this drift could be PMT aging, changes in temperature, oxygen leaking into the scintillator, or helium leaking into the PMTs [28]. To correct for time-dependent gain drift, a procedure was developed to fit the high energy background spectrum from a run to a spectrum obtained at the start of the data collection period, to determine the relative gain drift of the detectors over time. The high energy region was chosen as a strong signal was present from ^{40}K believed to originate from the phototube. At lower energies, the background spectrum shape may change over time due to time-varying external backgrounds present in Neutrino Alley (predominantly 511-keV γ -rays).

A RooKeysPdf [50] was generated from the first ninety-six hours of operation of each liquid scintillator cell. This RooKeysPdf was fit to every subsequent ninety-six hour period of data collection throughout the detector's operation allowing a single scaling factor to float. Following the fit, a spline was formed to interpolate the gain correction factor for individual runs within this ninety-six hour period. The relative gain curves were fit to the

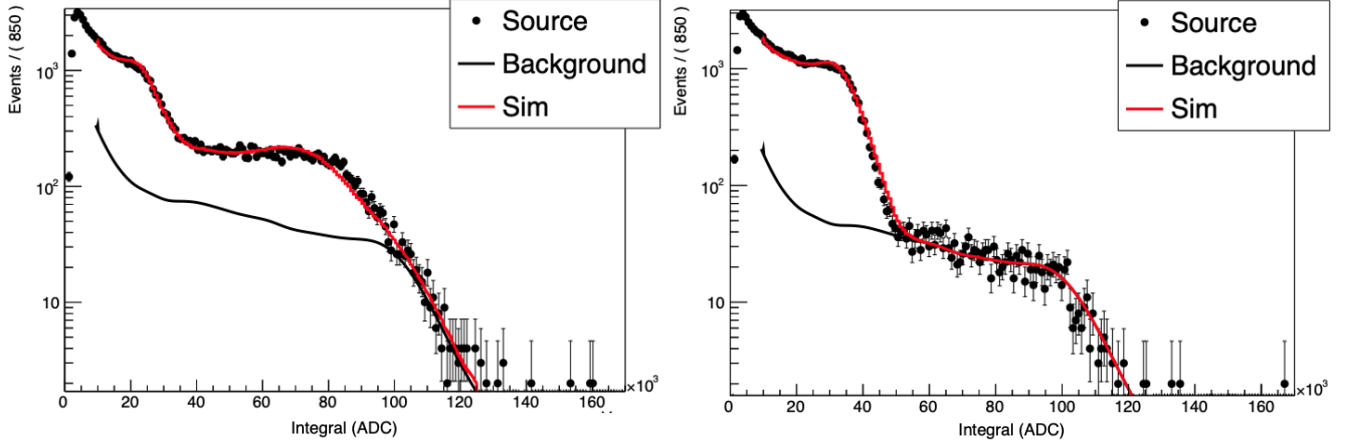


FIG. 6. Left: ^{22}Na calibration data along with smeared and fit simulated events. Right: ^{137}Cs calibration data along with smeared and fit simulated events.

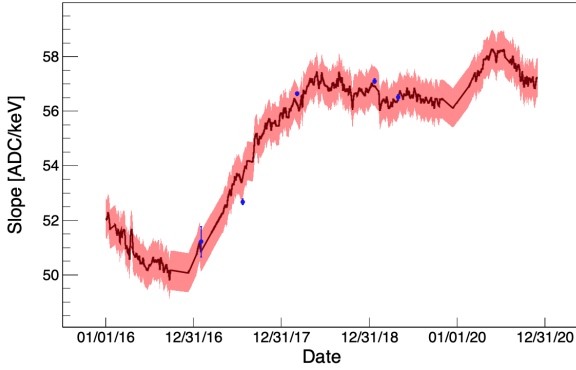


FIG. 7. Relative gain drift for a single detector (in black, uncertainty in red) from fitting the background spectrum of each ninety-six hour period of data collection, along with dedicated gamma calibrations for this detector (blue).

known absolute ADC-to-keV conversions determined by the dedicated gamma source calibrations. A plot of the gain drift over time, along with ADC-to-keV calibration parameters from dedicated source calibrations, can be found in Fig. 7.

C. Neutron calibration

A time-tagged ^{252}Cf source (produced at the Radiochemical Engineering Development Center (REDC) at ORNL) was used to identify a clean population of neutrons for optimizing PSD parameters and determining trigger efficiencies. For these runs, the time-tagged signal replaced the SNS timing signal in the data acquisition system, but otherwise the detector data acquisition con-

figuration remained unchanged. The PSD and timing distribution from this calibration is shown in Fig. 8.

Fig. 9 compares the spectrum from simulated ^{252}Cf

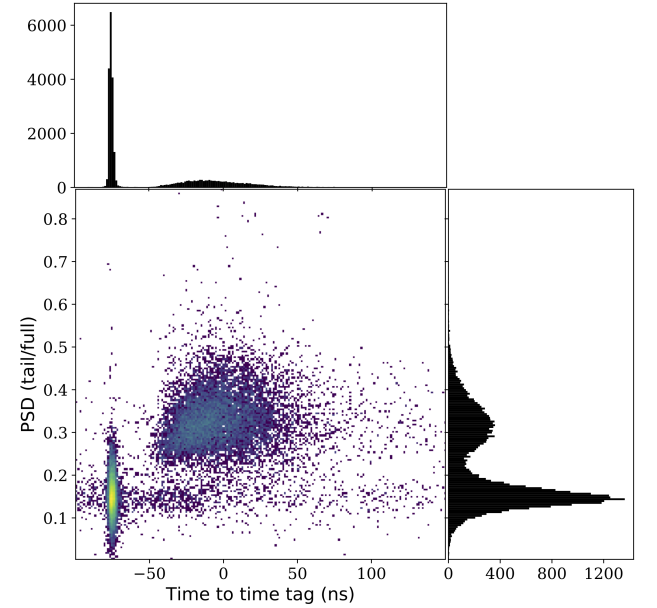


FIG. 8. Time of events in a liquid scintillator cell relative to the time-tagged decay compared to the PSD distribution. Gammas occur at approximately $t=-80$ ns, and neutrons occur between -50 to 200 ns.

events with those from the time-tagged ^{252}Cf run for a single channel. In both simulation and data, events are selected within a 140 ns window encapsulating the neutrons originating from the source. The simulation has energy resolution and trigger thresholds applied, and shows good agreement with the data.

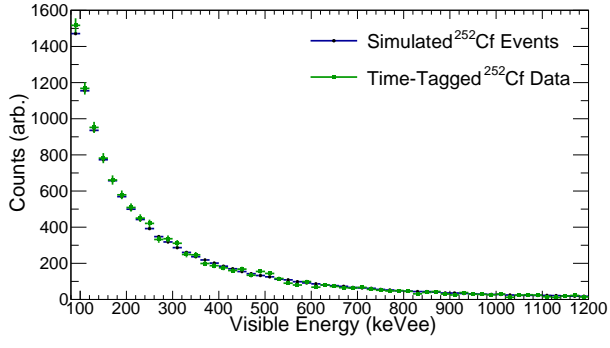


FIG. 9. Comparison of simulated ^{252}Cf events and data for a single channel. The simulation has energy resolution and trigger thresholds applied.